https://doi.org/10.1016/j.nanoen.2019.02.068



# Phonon Evidence of Kohn Anomalies in nanogenerator ZnO

Mingzi Sun and Bolong Huang*

*Department of Applied Biology and Chemical Technology, The Hong Kong Polytechnic University, Hung Hom, Kowloon, Hong Kong SAR, China*

*Email: bhuang@polyu.edu.hk

## Abstract

The origin of unique piezotronic properties within low dimensional nanomaterial systems will enable an in-depth understanding of nanogenerators for broad applications in the future. Notably, the low dimensional ZnO exhibits stronger temperature sensitivity than the bulk ZnO, which will be proved by the extreme phonon instability at room temperature 300 K. The temperature dependence shows a nearly Fermi-Dirac δ function. We have proposed the selection criteria for the nanogenerator material screening based on the theoretical derivation of *elastic perturbation entropy (EP-S)*. The resulted phonon conservation behaviors induced by the discontinuity in phonon dispersion dominates the highly sensitive response to the local electrical field change. The Kohn Anomalies (KA) has been identified in the wide bandgap semiconductor ZnO, in which discontinuous energy conversions induced by such KA or boundary discontinuity will not only minimize the degeneration effect but also induce the high piezotronic response. Moreover, we have carefully examined the ZnO surface on both structural and electronic structures, which identified the surface metallic properties. Thus, these theoretical results have supplied sound phonon evidence for the unique piezotronic properties in ZnO, which will facilitate the new insight in the future research of nanogenerators.

## Introduction

The invention of piezoelectric nanogenerator (PENG), triboelectric nanogenerator (TENG) and pyroelectric nanogenerator (PRNG) have significantly innovated the next generation nanotechnology for energy supply systems, which involves energy storage and harvesting, piezoelectricity, triboelectricity, and nanofabrication techniques [1-3]. Besides, many other applications based on the utilization of piezoelectricity are also attracting attentions, including solar cells, piezotronic transistor and even photocatalyst [4-7]. The prominent properties of nanogenerators endow great potential to break through the limitation by the conventional power supply system including immobility, limited lifetime, and safety risks [8-9]. Moreover, the self-power system can release the nanodevice from maintenance difficulty and extend their applications to small electronic devices, environmental monitoring, biomedical nanodevices [10-12]. Especially, the recently reported contact-electrification (CE) (or triboelectrification) phenomena has opened a novel direction for future energy storage and supply devices. Though this phenomenon has been discovered for over 2600 years in both heterogeneous or homogeneous material systems, the intrinsic mechanism is still under debate. Thus, a theoretical mechanism model for the origin of the unique piezotronic effect are pivotal that will be generally applied to explain all types of nanogenerator systems [13-15].

The first nanogenerator has been created based on the ZnO nanowire arrays due to their unique piezoelectricity caused by the atom scale polarization from non-centrosymmetric lattice structure [1]. ZnO, as an essential core of semiconductor research, shows 3.37 eV bandgap and high exciton binding energies, which have laid their foundation as competitive candidates in applications of electronical sensors and energy harvesting devices [16-17]. Abundant morphologies have been successfully synthesized with novel properties including nanowires, nanorods, nanobelts or even complicated structure as hierarchical structures, tetrapod and so on [12, 18-24]. However, compared with vast works on the synthesis and applications of nanostructured ZnO, the nature of the unique piezoelectricity has never been theoretically studied, which is pivotal in modifications of the properties [25-26]. The in-depth study of the corresponding quantum phenomena will not only assist the future optimization of the materials based on defect-engineering or structural modification but also accelerate the development of nanogenerators.

Presently, the transition between metal and insulator is usually dominated by two mechanism: one is the Peierls distortion induced by electron-lattice dynamics and the other one is the Mott transition induced by electric field screening of local electrons. However, the phonon related lattice vibration will also cause unique property alternation, which has been neglected in many researches. In low dimensional materials, the electron-phonon coupling (EPC) will strongly affect the dynamical nature of phonons and quantum electron transport [27-28]. The electron-phonon scattering induced by optical phonon has been proved that will interrupt the ballistic electron transport in materials [29]. In doped $Bi_2Se_3$, such electron-phonon interaction has induced an exotic new superconductor driven by a phonon-mediated mechanism [30]. With the reduced dimension of nanomaterials, phonons dispersion becomes pivotal in shaping the physical-chemical properties. The inharmonic lattice dynamics induced by the strong phonon interactions in $VO_2$ has been reported that dominated the first-order metal-insulator transition between the competing metallic and insulating phases [31]. Phonon as the collective media of quantization energy from lattice vibration will be

released by the vibration response. The quantum entanglement between phonon-photon interactions can also correlate to the optical properties of low dimensional materials. In 2D $WSe_2$, the strong coupling between photon in quantum dots and doubly degenerated phonons will lead to the realization of the quantum optomechanical platforms [32]. Empowered by the strong coupling between excitons and longitudinal optical phonons (LOPs), the net laser cooling in semiconductor materials has been achieved [33]. The abnormal behavior of phonon dispersion is known as Kohn anomalies (KA). This phenomenon usually will be found in metals that originated from the distortion of Fermi surface near the boundary [26]. For certain systems, KA will mediate the realization of metallization or even superconductivity through the phonon dispersion along different directions in the Brillouin Zone (BZ). KA usually correlate with the temperature $\boldsymbol{T}$ or wavevector $\mathbf{q}$. Particularly, on the high symmetry point such as Γ and K, strong Kohn anomalies at low frequency will significantly influence entanglement behaviors of phonon. For those temperature related KA, they will contribute to the strong piezotronics response that further lead to the application in nanogenerator. *This can be attributed to the KA induced discontinuity in phonon dispersion that will convert the mechanic energy to electrical energy. The normal continuous phonon dispersion will significantly deplete the mechanical energy by the non-conservative phonon behaviors that only result in the heat generation rather than electricity.*

Experimentally, Raman spectroscopy is the most commonly used indirect technique for investigating the lattice dynamic properties and electronic properties [34]. Yu *et al.* have assigned unidentified peaks of ZnO nanotube near 505 $cm^{-1}$ and 549 $cm^{-1}$ in Raman spectra to the surface defects [35]. However, another work of ZnO nanotube by Smith *et al.* demonstrated the 380 $cm^{-1}$ and 580 $cm^{-1}$ as the peaks of intrinsic defects [36]. Some abnormal phonon modes that ascribed to the enhanced phonon coupling are also detected in hydrogen/nitrogen implanted ZnO [37]. These results suggested the accurate determination of the defects in ZnO are still the open challenge. Thus, theoretical calculations and discussion on ZnO are the crucial steps to unravel the origin of their unique nano-piezoelectricity. The optical phonon can be theoretically calculated by various methods such as phonon zone folding (PZF), tight binding (TB) [38-39] and density functional theory (DFT) [40]. However, PZF failed to accurately describe the single wall nanotubes (SWNT) based on folding graphene [40]. The TB method relies too much on the empirical parameters in the literature that lead to a large mismatch in identifying such anomalies in phonon. In comparison, DFT, as an ab-initio method, can directly calculate the EPC effect without any externally or semi-empirically adjustable parameters. Surprisingly that, despite the vast literature on ZnO, first principle calculations of the very detailed temperature-dependent EPCs has not been systematically done so far, to the best of our knowledge.

Here, based on the density functional theory (DFT) calculations, we carefully calculated the phonon dispersion of ZnO with temperature dependence from 4 K to 800 K based on strict convergence criteria. The striking temperature-dependent anomalies have been found at room temperature (300 K) of ZnO semiconductors for the first time, which might be the dominant key to unravel the correlation between temperature-dependent quantized phonon anomalies and the origin of nano-piezoelectricity. This work has offered a comprehensive understanding of the properties of ZnO based on the thermodynamic description in correlation with Kohn Anomalies.

**Results and Discussion**

A series of DFT calculations have been operated on ZnO, ZnS, ZnSe, and ZnTe to investigate their unique piezotronic properties for an in-depth understanding of the anomalies for these materials.

In the phonon dispersion, we have phonon energy near the high symmetry **Γ** and **K** point function of the wavevector as:

$$E(q) = \hbar\omega_q = \alpha_\Gamma q + \hbar\omega_\Gamma + \mathcal{O}(q^2) \quad (1)$$

$$E(q) = \hbar\omega_{K+q'} = \alpha_K q' + \hbar\omega_K + \mathcal{O}(q'^2) \quad (2)$$

where, the $\omega_q$ represents the phonon frequency at the highest optical branch at wavevector **q**. Due to the high symmetry of these two points, the shape of the highest optical branch flat at point **Γ** and **K**, indicating an analytic behavior of the dynamic matrix dependence on wavevector **q**. However, we observe the non-analytic behaviour in low dimensional ZnO. At **Γ** point, it is noted that the split to an upper longitudinal optical (LO) branch and a lower transverse optical (TO) branch. The temperature-dependence phonon dispersion has been calculated based on the different convergence of Fermi energy perturbation on the 2D ZnO (**Figure 1)**, in which we have emphasized the striking discontinuity feature at the representative high symmetry Gamma point. The abnormal drop of 300 K can be observed in the combination of all the frequencies at Gamma point at a different temperature from 4 K to 800 K (**Figure 1a**), which becomes more evident based on more strict convergence (**Figure 1b)**. However, it is noted that the linewidth near Gamma point is temperature independent. which remained unchanged from 4 K to 800 K. This finding demonstrates the competition between EPC and the increased phonon–phonon interactions induced by anharmonicity will offset each other to the final balance.

By plotting the temperature dependence of frequency at Gamma point, a series of minor kink from 4K to 800 K including a dominant kink at 300 K can be clearly observed even with different convergence (**Figure 1c-1d**). By carefully examining the specific range, the dominant discontinuity at 300 K shows the frequency of 565 $cm^{-1}$ with a nearly 20 $cm^{-1}$ drop in the strict convergence and the frequency of 580 $cm^{-1}$ in normal convergence calculation, which are both close to the abnormal vibration modes in previous experiments [35-36] (**Figure 1e**). This difference indicating the strong sensitivity of local phonon vibration mode to the temperature change can only be detected under highly accurate calculations. Based on the temperature sensitivity at low dimensional ZnO, we further develop the phonon energy *E(q)* of piezotronic materials from simple function related to wavevector **q** to a more detailed function *E(q, T)* that related to both wavevector **q** and temperature **T**. Thus, the general expression of phonon energy for piezotronic materials for nanogenerators can be derived as follow,

$$\Delta E(q,T) = \hbar\Delta\omega = \hbar\int\frac{\partial\omega_q}{\partial q}dq + \hbar\int\frac{\partial\omega_q}{\partial T}dT \quad (3)$$

In the low dimensional materials, the phonon energy is highly dependent on the temperature sensitivity to the temperature, that the wavevector part would be nearly to zero. Meanwhile, such sensitivity to **T** will be much alleviated in bulk materials, in which the sensitivity to wavevector **q** is more dominate. Thus, a further look into the derivate of the temperature dependence of frequency has proved the sensitivity to

temperature in low dimensional ZnO, in which the discontinuity point near 300 K becomes evidently exceptional from other temperature (**Figure 1f**). According to the extreme abnormal phonon dispersion at 300 K, the phonon dispersion on temperature will be considered as the Dirac δ-function, which usually describe the discontinuous distribution of energy that concentrate at a transient point.

The near Fermi–Dirac δ function behaviour suggests that near the high symmetry point, the phonon dispersion behaviour is elastic with conservative phonons based on ultra-low energy loss (**Figure 1g**). Usually, the normal non-conservative dispersion with high phonon dispersion will significantly annihilate the electrons that leads to very low or none response of the electrical field induced by mechanical force [41]. These findings arise a new question that such conservative phonons behaviors appear in most nanomaterials or only specific type of materials. However, the detection of such unique property is still not easy since the emerging surface defects have buried the phonon dispersion. Moreover, we have summarized the temperature point with the discontinue phenomenon in strict convergence that revealed a nearly linear and discrete behavior, namely a "quantized anomalies", which indicates that the only at certain temperature the unique piezotronic behaviour will appear (**Figure 1h**). Such quantized anomalies widely exist along the temperature and reaches the maximum at 300 K for low dimensional ZnO. Therefore, the low dimensional ZnO will exhibit a discontinuous energy conversion to the local electrical field induced by the KA that will lead to the conservative phonon dispersion, which can explain the exceptionally high response of the piezotronic effect.

To support our DFT calculation findings, we also investigate the phonon dispersion from theoretical derivation. For a specific system, take the one-dimensional case, the force is related to the displacement $x$ as $F = Dx$, where D is the force constant and $x$ is the displacement distance. Generally, the force has been considered as the function of position only, which can be represented as the derivative condition.

$$F(x) = -\frac{\partial E}{\partial x} \tag{4}$$

The total energy calculated in the work has considered the temperature effect as $E_{total} = E - TS$ . The application of Eq. (5) to the expression of force-constant ($D$) is given as:

$$D = \frac{\partial^2 E}{\partial x^2} = \frac{\partial^2 E}{\partial x^2} - \frac{\partial^2 (TS)}{x^2} \tag{5}$$

Note we omitted the contribution of higher order derivatives. The Eq. (5) can be fully derived as:

$$D = \frac{\partial E^2}{\partial x^2} - \frac{\partial^2 (TS)}{x^2} = \frac{\partial E^2}{\partial x^2} - \frac{\partial}{\partial x}\left(T\frac{\partial S}{\partial x} + S\frac{\partial T}{\partial x}\right) = \frac{\partial^2 E}{\partial x^2} - \left[\frac{\partial S}{\partial x}\frac{\partial T}{\partial x} + S\frac{\partial^2 T}{\partial x^2} + \frac{\partial T}{\partial x}\frac{\partial S}{\partial x} + T\frac{\partial^2 S}{\partial x^2}\right] \tag{6}$$

Assuming T is independent to the oscillation displacement $x$, then Eq. (6) will give:

$$D = \frac{\partial^2 E}{\partial x^2} - T\frac{\partial^2 S}{\partial x^2} \quad (7)$$

We now simply and directly express the D following by the full set of state-function $D(q, \omega, T)$ as:

$$D = D(q, \omega, T) = \int \frac{\partial D}{\partial q} dq + \int \frac{\partial D}{\partial T} dT + \int \frac{\partial D}{\partial \omega} d\omega = \int \frac{\partial D}{\partial T} dT \quad (8)$$

However, for nearly-harmonic oscillation, the D is independent to the wave-vector, $q$, and frequency, $\omega$. Combining Eq. (7) and Eq. (8) yields:

$$\frac{\partial D}{\partial T} = \frac{\partial}{\partial T}\left(\frac{\partial^2 E}{\partial x^2}\right) - \frac{\partial^2 S}{\partial x^2} - T\frac{\partial}{\partial T}\left(\frac{\partial^2 S}{\partial x^2}\right) \quad (9)$$

Assuming the second ordered derivative form of as-given geometric configuration enthalpy $\frac{\partial E^2}{\partial x^2}$ is independent to T, and applying A to represent $\frac{\partial S^2}{\partial x^2}$ , then Eq. (9) will be updated as:

$$\frac{\partial D}{\partial T} = -A - T\frac{\partial A}{\partial T} \quad (10)$$

Defining *i* is the *i*th temperature T correlated discontinuity point of phonon dispersion curve. Then the Eq. (10) is summed over with *i* as follow:

$$\sum_i \frac{\partial D}{\partial T} = \sum_i \left(-A - T\frac{\partial A}{\partial T}\right) = -\sum_i \delta(T - T_i) \quad (11)$$

To cancel the infinity of δ-functions, we can integrate Eq. (11) to the followings:

$$\int A\, dT + \int T\frac{\partial A}{\partial T} dT = \int \delta(T) \quad (12)$$

$$2AT = Constant \quad (13)$$

By representing *Constant* by *C* and extend the expression of *A*, we can have:

$$A = \frac{C}{2T} \to \frac{\partial^2 S}{\partial x^2} = \frac{C}{2(T - T_i)} \quad (14)$$

The vibration entropy *S* will be expressed as:

$$S(T,\omega) = k\left\{\int \frac{\hbar\omega/kT}{\exp\left(\frac{\hbar\omega}{kT}\right)-1}F(\omega)d\omega - \int F(\omega)ln\left[1-\exp\left(\frac{-\hbar\omega}{kT}\right)\right]\ d\omega\right\} \quad (15)$$

Therefore, the expression of $C$ will be presented as:

$$C = 2kT\frac{\partial^2}{\partial x^2}\left\{\int \frac{\hbar\omega/kT}{\exp\left(\frac{\hbar\omega}{kT}\right)-1}F(\omega)d\omega - \int F(\omega)ln\left[1-\exp\left(\frac{-\hbar\omega}{kT}\right)\right]\ d\omega\right\} \quad (16)$$

Since the configuration entropy $S = k_B lnW_i$, Eq. (14) can also be derived as:

$$\sum_i S_i = \sum_i (k_B \ln W_i) = \sum_i \frac{C}{2(T-T_i)}\ x^2 \quad (17)$$

$$\sum_i (\ln W_i) = \sum_i \frac{C}{2k_B(T-T_i)}\ x^2 \quad (18)$$

As $\sum_i(\ln W_i)$ describe the disorder level of the local harmonic perturbation, Eq. (17) can be considered as the definition of *elastic perturbation entropy (EP-S)* that indicates a clear dependence on both temperature $T$ and the perturbation displacement $x$. It is noted that $T$ and $x$ display a converse relationship with the *EP-S* that will lead to the different direction of phonon behaviors or even structure changes. To further define the criteria to screen the potential nanogenerator materials, we will limit Eq.(17) as $x$ approaching zero while $T$ approaching $T_i$.

$$\lim_{\substack{x\to 0\\ T\to T_i}} \ln W_i = \lim_{\substack{x\to 0\\ T\to T_i}} \frac{C}{2k_B}\frac{x^2}{(T-T_i)} = 0 \quad (19)$$

For piezoelectricity and non-piezoelectricity materials under non-constrained condition, the reversible energy (at least over 100,000 times reversibility) requires the convergence of $\sum_i(\ln W_i)$ to zero during the operation period. From mathematical perspective, this demonstrates that the convergence of the numerator perturbation displacement $x$ should be faster than the denominator $(T-T_i)$. Thus, the sudden extreme change of phonon entropy will be completely depleted by the nonconservative phonon scattering. This suggested that the guarantee of the successful operation of nanogenerators should be based on the requirement of frozen phonon at specific points. However, sudden infinite increase of $\sum_i(\ln W_i)$ as well as the EP-S will occur when temperature $T$ close to $T_i$. These specific temperature points will be considered as the energy maximum depletion points for piezoelectrical materials. Similar situation will also happen when the nanogenerator materials becomes fatigue after long-term operation, the convergence of denominator $(T-T_i)$ will become faster that lead to infinite increase of EP-S, which usually will result in the irreversible displacement of

atoms in the structure. However, due to the lack of a large amount of experiment analysis, the present characterization of the fatigue condition in nanogenerator is still very limited. Through theoretical derivation, in this situation, the perturbation displacement *x* will become larger than the elastic-harmonic displacement limits as $L_0$. The induced sudden extreme change of entropy will lead to the structural instability with the large displacements of atoms in the lattice. The evident deviation behaviors of atoms will further induce the formation of defects including vacancies, interstitials, anion-Frenkel defects and Schottky defects, etc. Thus, the further classified criteria for piezoelectricity material are listed below based on Eq. (18) as:

$$\begin{cases} \lim\limits_{\substack{x\to 0 \\ T\to T_i}} \ln W_i = 0 & 0 < x < L_0 \\ \lim\limits_{\substack{x\to 0 \\ T\to T_i}} \ln W_i = \infty & L_0 < x < \infty \end{cases} \tag{20}$$

Within the criteria, $L_0$ represents the *largest elastic perturbation range* in varied temperature that induced by the local perturbation electrical field. $L_0$ should be an intrinsic material property that only decided by nature of material and the temperature. When the perturbation displacement *x* is less than $L_0$, the phonon behavior is reversible with phonon conservation that will lead to nearly zero energy depletion by the phonon scattering. Such low energy depletion will lead to a high response of the energy conversion from mechanic to electricity. The perturbation displacement *x* is independent of the temperature that only affected by the *EP-S*. With this selection criteria, screening the potential candidates for nanogenerator will be extended beyond the piezoelectrical materials and considered from a quantum phonon perspective. This can also support the recent finding in monolayer $MoS_2$ and ZnS for energy conversion and piezotronics by Wang *et al.* [42-43].

The key feature of piezoelectrical material is the induced local electrical field by the applied force. To figure out the correlation between the electrical field and the piezoelectrical response, here, we combine the thermodynamic concept and the induced electricity of the perturbation as follows:

$$dG = -TdS = -QdU \tag{21}$$

where *G* is the Gibbs free energy and *U* is the piezoelectric potential. By combining Eq. (12), we can derive the correlation between electrical potential and the perturbation displacement *x* as:

$$U = \frac{C}{Q} x^2 \tag{22}$$

where we define the *Q* as the induced local *perturbation electrical charge* of applied force on piezoelectricity material. By collaborating with the piezoelectricity potential expressions from previous work [44], Eq. (22) will become:

$$\frac{C}{Q} x^2 = \frac{qN}{2\varepsilon_s} x^2 \tag{23}$$

The $q$ is the electronic charge induced by direct mechanical force and $\varepsilon_s$ means the the permittivity of the material. *N* is the concentration of charge carriers. By combining the expression of *C* from Eq.(14), we can derive as follows:

$$\frac{\partial^2 S}{\partial x^2} = \frac{qQN_A}{4\varepsilon_s T} \quad (24)$$

$$S = \frac{qQN_A}{8\varepsilon_s(T - T_i)}\ x^2 \quad (25)$$

By this correlation, the *EP-S* will not only relate to the perturbation displacement *x* and temperature *T*, but also the perturbation electrical charge. The *Q* will depend on the electrical response that will be largely enhanced by the existence of KA. This correlation is consistent with the expression of potential distribution dependence on the depletion widths with further extension on the *perturbation electrical charge Q* [13-15, 44-47].

To introduce the quantum concept into our general mechanism, we apply the quantum energy expression to Eq. (21) will have:

$$dG = -TdS = -\hbar\ (n + \tfrac{1}{2})\ d\omega \quad (26)$$

where $\hbar$ is the Planck constant and *n* is the quantum number. The further adoption of the full expression of *S* from Eq. (15) will lead to:

$$S(T,\omega) = \frac{\hbar\omega}{T}(n + \frac{1}{2}) \quad (27)$$

$$\tilde{\omega}(q,T) = \frac{S(T,\omega)\ T}{\hbar(n + \frac{1}{2})} \quad (28)$$

Through the mathematical approximation, the relationship between ω and T are non-analytic, indicating a discontinuous illustration as **Figure 1h**. *This is consistent with our phonon evidence of the discontinuity in low dimensional ZnO, representing a quantum nature of the energy conversion in nanogenerator.* However, the present challenge of the accurate description of the correlation between phonon dispersion and temperature through experiment is still existing. Our theoretical calculations and derived general piezoelectricity mechanism will facilitate to explain some key concerns in energy conversion systems, especially the nanogenerator. For the first time, we apply the phonon concept in microscopic quantum perspective to support the proposed mechanism in nanogenerators by Prof. Wang.

To further precisely describe the KA, we also computed highly accurate phonon dispersion with over 2000 dense k points to investigate the phonon vibration in the bulk ZnO materials for a comprehensive interpretation of the origins of the anomalies. Notably, the optical branch and the acoustic branch have a scale around 150 $cm^{-1}$ and 250 $cm^{-1}$, respectively (**Figure 2a**). There is a gap around 150 $cm^{-1}$ between optical branch and acoustic branch. Several kinks can be found at different wavevector that is in accordance with our previous conclusion that phonon dispersion in bulk ZnO will be sensitive to the wavevector **q** rather than temperature. In particular, we can observe the discontinuity near the Gamma point with the frequency of 520 $cm^{-1}$ by the enlarged phonon dispersion display, which is close to the anomalous peak identified in Raman spectra [35] (**Figure 2b**). Another discontinuity near wavevector of 0.390 has weaken

the degeneration effect of some vibration modes (**Figure 2c**). The further minimization to the degeneration effect could be further proved by the kink near wavevector of 0.466 (**Figure 2d**). Both turning point noted at wavevector of 0.885 and 0.408 will switch off degeneration of the vibration mode as well (**Figure 2e-2f**). The combination of all these evident discontinuity in phonon dispersion will be considered as the fingerprint of Kohn Anomalies, which will significantly reduce the degeneration effect that enlarge the response to the piezotronic effect. Therefore, we have identified such unique anomalies in wide bandgap semiconductor materials for the first time, which usually only occur in metal materials.

Moreover, the phonon dispersion of ZnS also has been presented, which has shown much more abnormal kinks than that of bulk ZnO, especially in the acoustic branch (**Figure 3a**). The scale of optical branch and acoustic branch, as well as the gap between them, all shrink in phonon dispersion of bulk ZnS. Moreover, the concave kink at the extreme point near Gamma point in ZnO becomes convex in ZnS with the similar 0.5 $cm^{-1}$ drop of frequency (**Figure 3b-3c**). Near the boundary, it is noted that a gap induced by the complete disappearance of degeneration locates near wavevector of 0.95 in the optical branch (**Figure 3d**). The existence of discontinuity is widely distributed along the whole wavevector, which can be seen even near the boundary of the optical branch (**Figure 3e-3f**). The In particular, both low frequency and high frequency of optical branch display similar symmetrical kinks near the wavevector of 0.998 induced by the boundary scattering (**Figure 3g-3h**). The Kohn anomalies can be seen at the low wavevector (**Figure 3i-3j**). At the lower wavevector near 0.3, the scale of kinks that are nearly 1 $cm^{-1}$, which becomes more apparent than that at the higher wavevector (**Figure 3k**). A continuous combination of obvious degeneration and non-degeneration implies that the weak continuity cannot entirely eliminate the degeneration effect (**Figure 3l**). In comparison with the optical branch, several discontinuities become notable in acoustic branch near the wavevector of 0.3 and 0.4 (**Figure 3m-3n**). The frequencies near 0.3 wavevector experience a nearly sudden 5 $cm^{-1}$ drop and increase at the same point. Similar with the optical branch, one strong and one weak discontinuity will be found near the boundary of the acoustic branch at the wavevector of 0.9 (**Figure 3o**). However, at the higher frequency at the same wavevector, the degeneration effect appeared due to the scattering of symmetrical point (**Figure 3p**). Similar KA have also been presented in ZnSe and ZnTe in the supporting materials (**Figure S1-S2**).

A careful and combined examination of all the phonon dispersions in bulk materials is presented. The phonon dispersion of bulk ZnSe and ZnTe are also calculated for comparison with the ZnO and ZnS (**Figure 4a-4d**). Notably, the scale of the optical branch and acoustic branch of phonon dispersion further reduced, where the gap between the two branches is disappearing (**Figure 4c-4d**). However, the discontinuity in phonon dispersion is becoming more intense than ZnO and ZnS. Moreover, both ZnSe and ZnTe exhibit discontinuity the highest frequency at Gamma point with a sudden increase rather than the drop of frequency discovered in ZnO and ZnS. In addition, the derivations of temperature dependence of frequency support that the discontinuity scale is becoming much larger in ZnS and ZnSe (**Figure 4e-4h**). The 2D mapping of phonon dispersion will further demonstrate the asymmetry near all the discontinuity or Kohn anomalies in the phonon dispersion, indicating the non-centre symmetrical structure of all the lattices. These results will drive us to answer the question of where the origins of these asymmetrical structures are. Compared with the low-dimensional ZnO calculation results, we can deduce that the abnormal phonon

dispersion is much more evident in low dimensional ZnO rather than bulk materials. Besides the synthesis routes, the surface phonon instability effect will be another vital origin of the surface defect, which will explain the induced abnormal high piezotronic response for the application in piezotronics nanodevices.

As the most important ZnO surface, we have chosen the (0001) surfaces to investigate the electronic structures and defect formation. The relaxed surface structure has shown an evident surface distortion, especially the oxygen extrusion (**Figure 5a**). Similar evident oxygen extrusion will also be observed in the with ab-initio MD method under 300 K (**Figure S3**). Through the total density of states (PDOS) at different temperature shows, we always observe that the Fermi level locates near the conduction band minimum (CBM), indicating a surface metallic property (**Figure 5b**). This result is also supported by the TDOS of ZnO along different time in MD simulations (**Figure S4**).The surface distortion will further potentially induce the new reconstruction that has been further proved by the STM simulation image (**Figure 5c**). Interestingly, the HOMO-LUMO 2D mapping also support the surface distortion by the p-d orbital interaction behaviors between Zn and O atoms (**Figure 5d**). By the further detailed illustration and analysis of the oxygen extrusion with varied coordinated Zn atoms in the lattice, we will find that the gap states gap states orbitals predominantly localized on over/under coordinated Zn rather than contributed from 3-fold planar Zn (**Figure S5-S7**).

Our previous theoretical calculations have proved the non-existence of pure ZnO in low dimension. Previous experiments also classified the abnormal vibration modes in Raman spectra to the intrinsic defects. Hence, the formation of intrinsic defects on the surfaces are essential to correlate with the abnormal phonon behaviors. As shown in **Figure 6a**, the formation of oxygen vacancy ($V_O$) in will leave the two excess electrons localized near the first neighboring Zn sites on the topmost layer with two different spin directions. In contrast, the localized hole states by the formation of zinc vacancy ($V_O$) localized on the third nearest neighboring O-sites with orbital direction preferences (**Figure 6b**). $V_{Zn}$ tends to stabilize the surface under Zn-poor limit as the removal of Zn leads to decrease the number of electrons in the surface state as the key role on stabilizing the (0001) polar surface instead of the charged $V_{Zn}$. Beside the zinc vacancy, zinc adatom ($A_{Zn}$) has also been calculated, in which the excess electrons from 3d-orbitals and 4s-orbitals carried by $A_{Zn}$ localized on the three first nearest neighboring Zn-sites (**Figure 6c**). Similarly, we also consider the effect of oxygen adatom ($A_O$) sitting on the top Zn-O bilayer. With the formation of $A_O$, the two different spin directions of the localized gap states distributed on the ZnO(0001) surface. The p-π orbitals always localize on the $A_O$ site (**Figure 6d**). For the pristine ZnO with surface distortion, the orbitals are localized directly on the surface oxygen extrusion areas. In accordance with the orbital distribution, the TDOS of all defects are demonstrated (**Figure 6f**). The formation energies of point defects are compared in O-rich and O-poor environment, respectively (**Figure 6g-6h**). Unlike the case in bulk ZnO, our calculations show that the neutral oxygen vacancy ($V_O^0$) is not the lowest energy defect in ZnO(0001) surface system. For O-rich environment, $V_{Zn}$ in neutral state is the second lowest cost defect and shows close formation energy with $A_O$, which lead to a compensation between each other due to the distinct charge coupling based on an opposite electronegativity. Moreover, in both O-poor and rich conditions, the $A_O$ is always the most stable defect that remains at the neutral state. Combine with the case of $V_{Zn}$ under both O-poor and O-rich conditions, we found the consistency that the $A_{Zn}$

is energetically favorable to form under O-poor while $V_{Zn}$ is more easily formed under O-rich condition. With the MD simulations, we also compare the surface dipole moments and system total energies of surface structures at different points in time, based on the ideally truncated original bulk-like ZnO(0001) surface (**Figure S8**). As the simulation time increase, the surface energy displays an increase trend while the dipole moment will experience a fluctuation. Notably, the variation trend of surface dipole moment and system total energy are indeed reverse at the initial MD simulation. This suggests that the stabilization of the surface will be achieved by the comprise the dipole moment. The features of "eyes" observed the STM experiments on Zn-terminated ZnO(0001) surface consist of a bright spot with a dark ring and a bright broadened strip in turn around. The DFT-based STM simulations have been operated to interpret the steric mechanism of these eyes and structures (**Figure 7**). The previous experiment finding gave a good trend corresponding to our formation energy levels of native defects calculations, as we confirm that $A_O$ is the most easiest defect formed under both O-poor and rich limit, and $A_{Zn}$ is the second easiest one formed under Zn-rich (O-poor) limit [48]. Detailed analysis of STM of $A_O$ and its comparison with the experiment are illustrated in **Figure S9**.

In summary, this work presents an unusually strong temperature dependence of phonon dispersion in the low dimensional ZnO, which is firmly correlated to the high response to the local electrical field. The phonon instability on the low dimensional ZnO surface will be induced by the large transient change of *EP-S*. More importantly, such phonon behaviors offered a plausible explanation for the unidentified surface defects in conventional characterizations. The abnormal KA phenomenon is noted in bulk semiconductor materials, especially at high symmetry point and BZ boundaries. By a comprehensive probe on the native defect states on the Zn-terminated ZnO(0001) polar surface, we proposed that it is the surface defect states or extrinsic dopants effect that overwhelm the intrinsic p-type conductivity and transport of the ZnO bulk system that leads us a long interest and difficulties to achieve. Therefore, the solid phonon evidence of KA in ZnO with the intrinsic defect formation have supplied a general mechanism from phonon perspective. This work will benefit our understanding of the intrinsic nature of nanogenerator as well as the correlation with the defective structure of ZnO.

**Acknowledgements**

The author BH gratefully acknowledges the support of the Natural Science Foundation of China (NSFC) for the Youth Scientist grant (Grant No.: NSFC 21771156), and the Early Career Scheme (ECS) fund (Grant No.: PolyU 253026/16P) from the Research Grant Council (RGC) in Hong Kong.

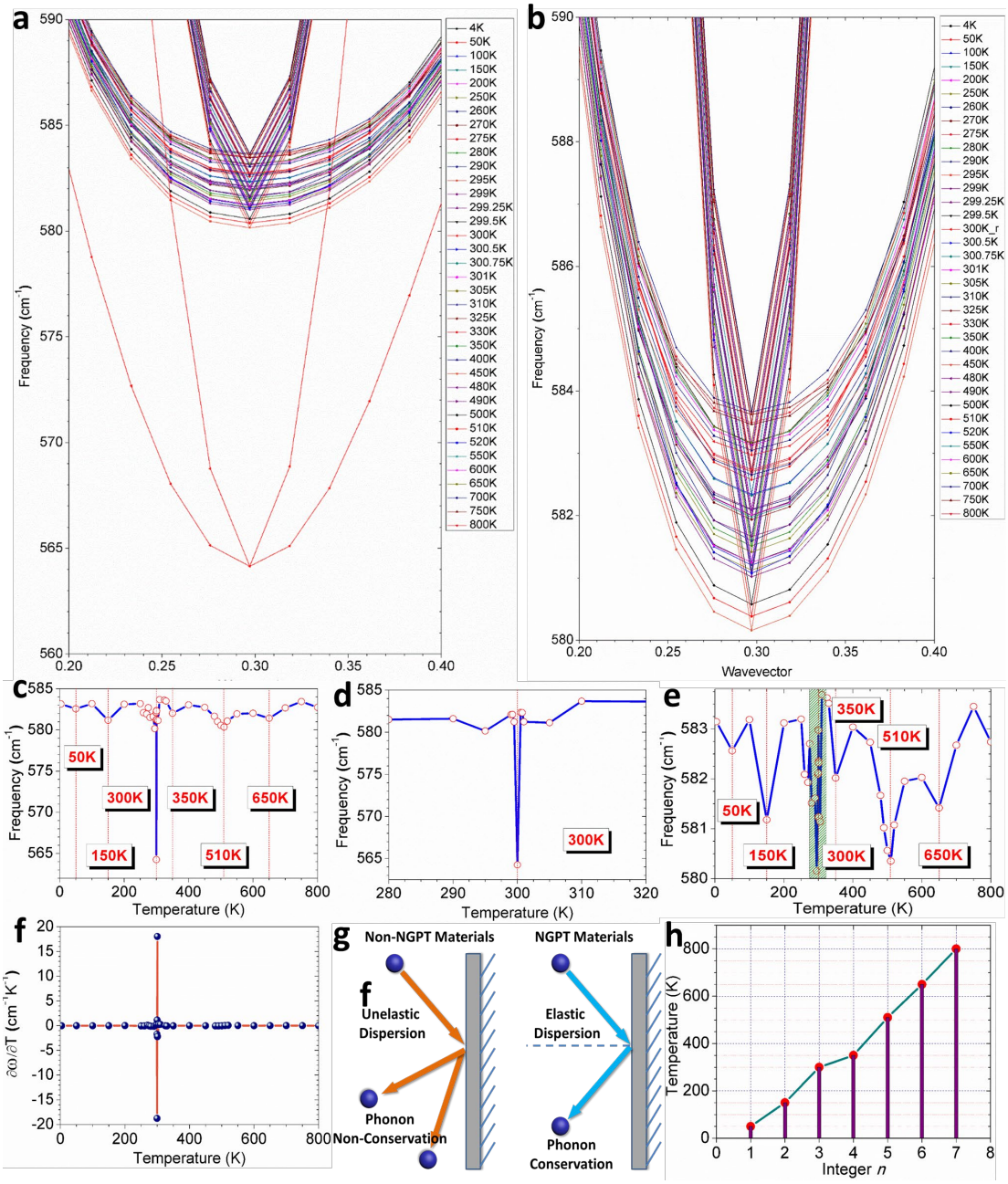


**Figure 1.** Temperature dependence of band structure of ZnO with more strict convergence of Fermi level. Frequency dependence on temperature from 4 K-800 K based on (a) normal convergence and (b) high convergence of DFT. The dependence of frequency at Gamma point on temperature from (c) 4 K- 800 K and enlarged range of (d) 280 K- 320 K. (e) The dependence of frequency at Gamma point on temperature from (c) 4 K- 800 K based on normal convergence of DFT. (f) The derivative of frequency on temperature from 4 K- 800 K. (g) The dispersion behaviors difference in non-NGPT and NGPT materials. (h) The "quantized anomalies" discovered based on anomalies at temperature variation.

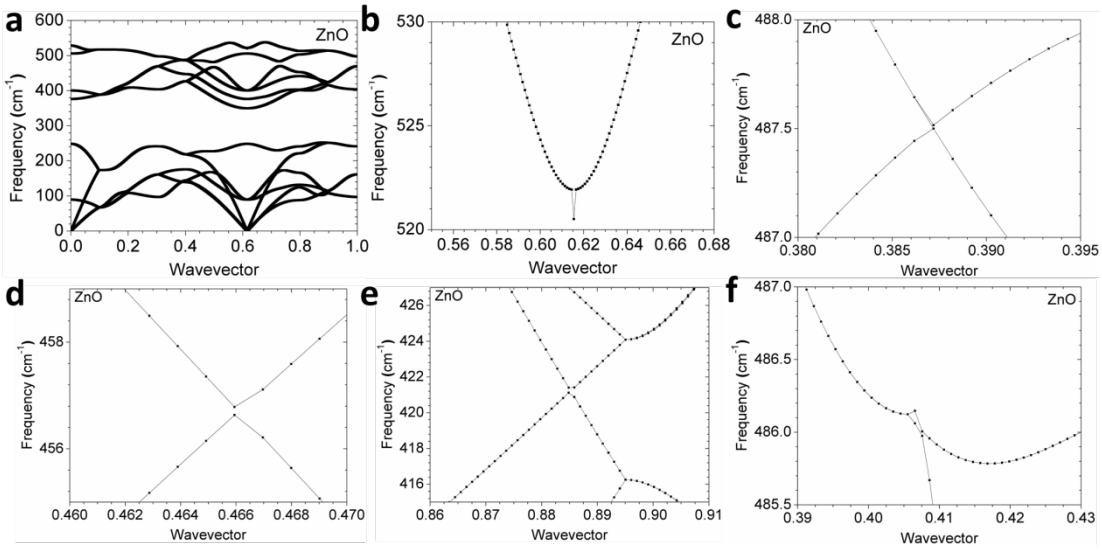


**Figure 2.** The phonon dispersion of bulk ZnO. (a) The overall phonon dispersion of bulk ZnO. (b)-(f) The enlarged illustration of ZnO abnormal kinks in the phonon dispersion at different wavevectors.

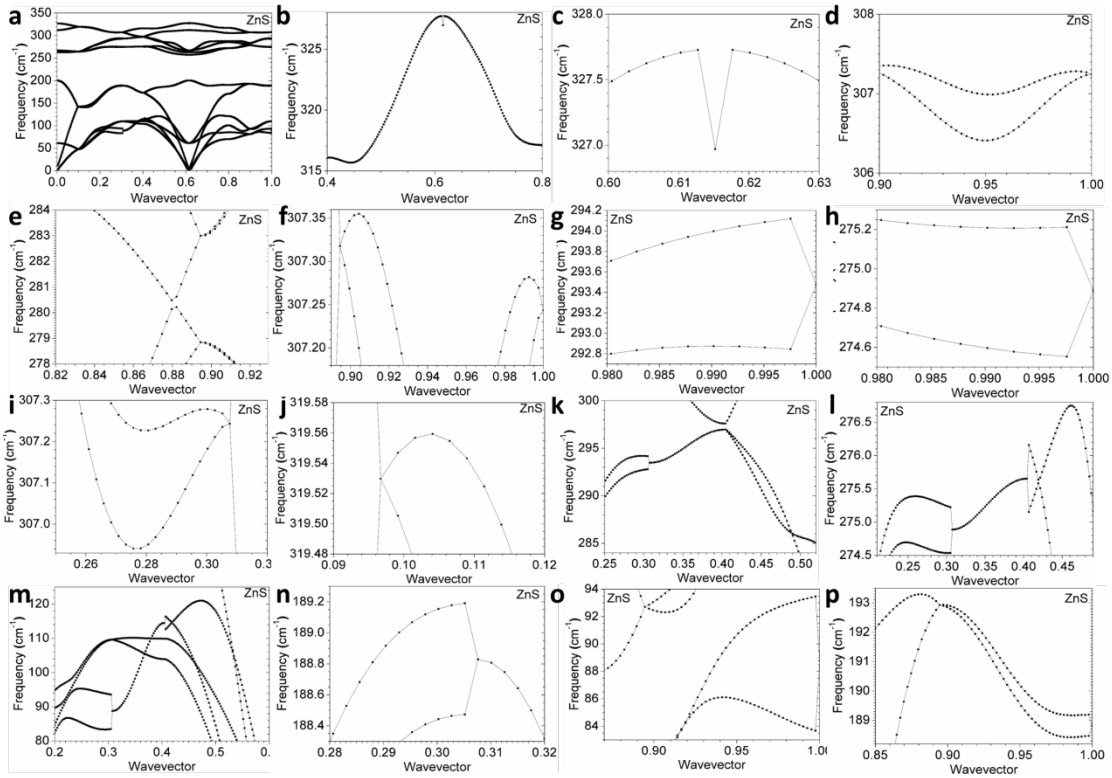


**Figure 3.** The phonon dispersion of bulk ZnS. (a) The overall phonon dispersion of bulk ZnS. (b)-(l) The enlarged illustration of ZnS abnormal kinks in the optical branch of phonon dispersion. (m)-(p) The enlarged illustration of ZnS abnormal kinks in the acoustic branch of phonon dispersion.

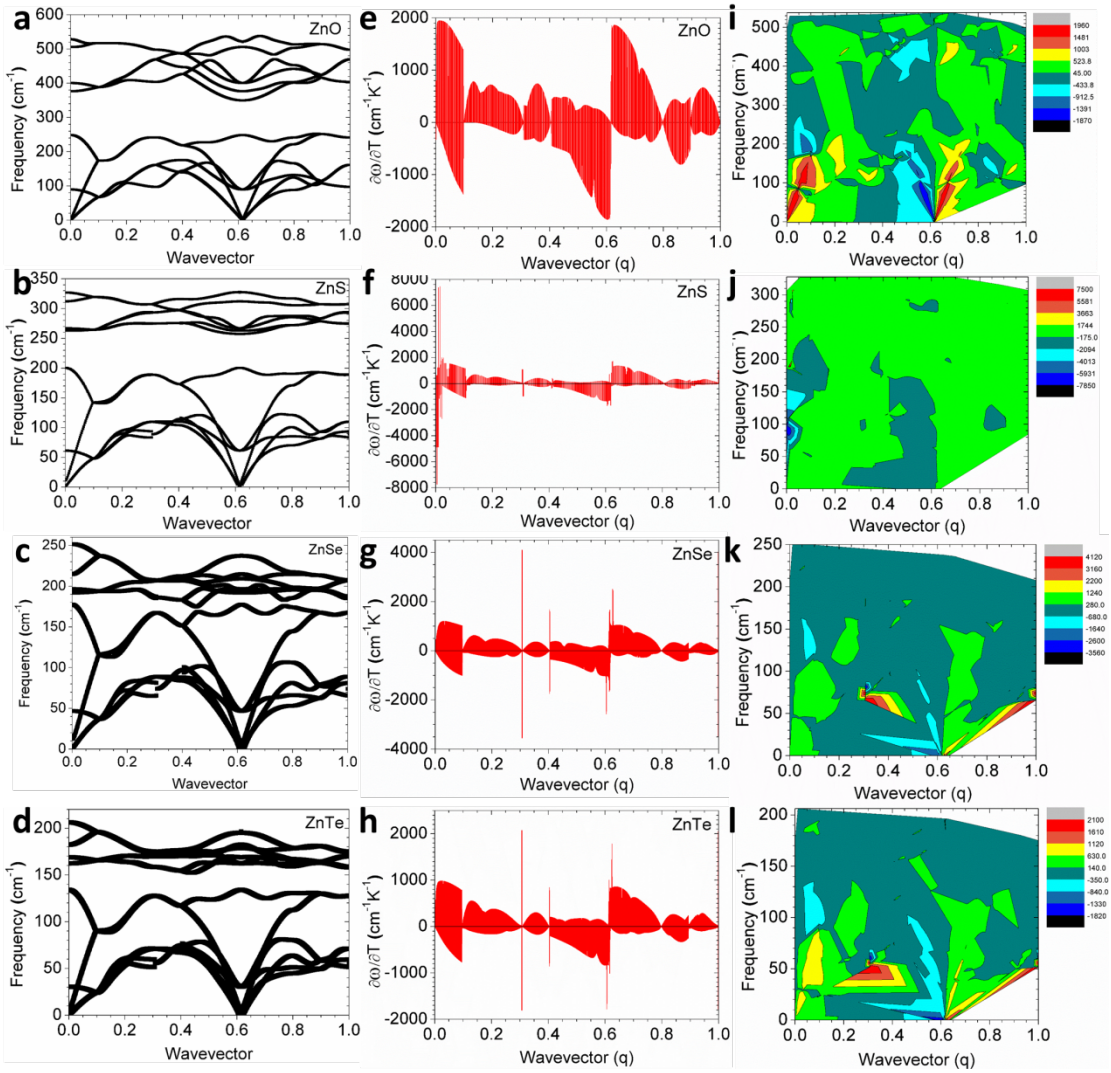


**Figure 4.** The combination phonon dispersion behaviors of bulk ZnO, ZnS, ZnSe and ZnTe. (a)-(d) phonon dispersion, (e)-(h) temperature dependence of frequency. (i-l) 2D mapping of phonon dispersion.

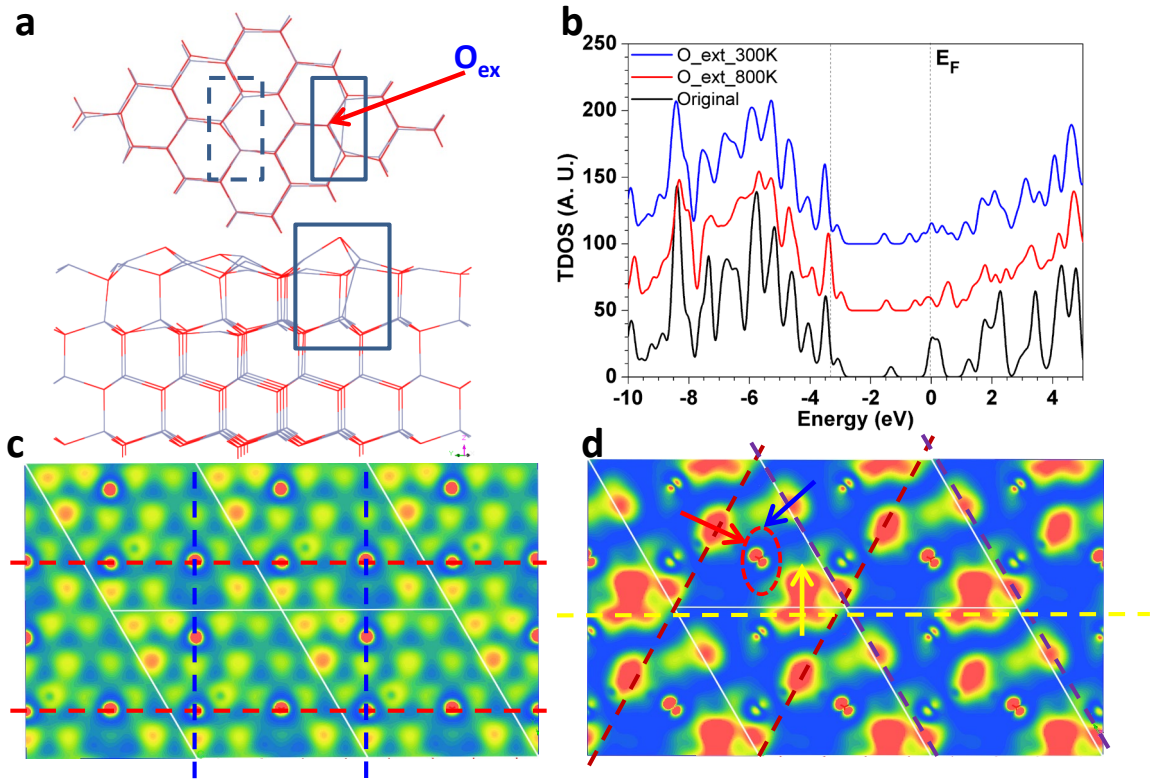


**Figure 5.** The structural and electronic structures of ZnO (0001) surfaces. (a) Top view and side view of ZnO (0001) surfaces. (b) The TDOS of ZnO at different temperature. (c) The STM simulation of ZnO (0001). (d) The top view of 2D HOMO/LUMO mapping of ZnO (0001) surfaces.

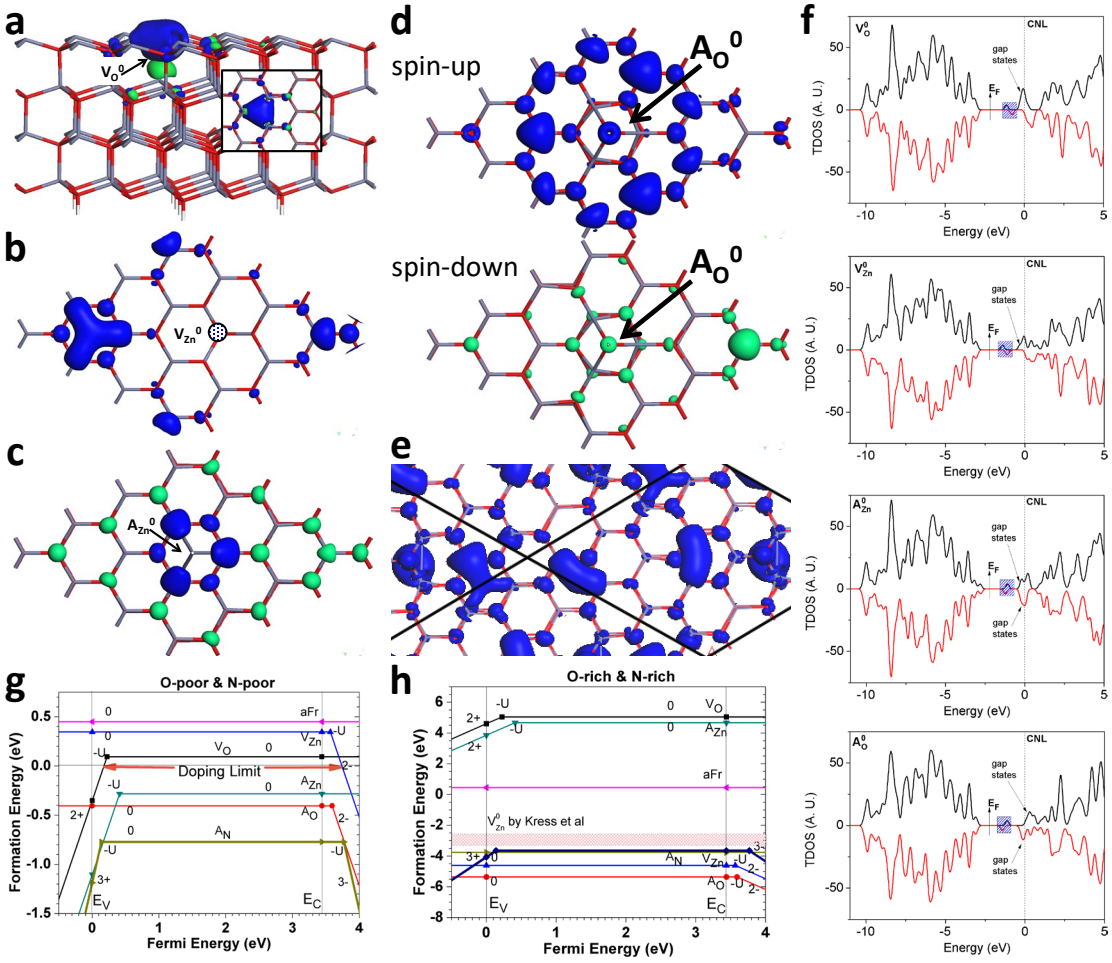


**Figure 6.** The investigation intrinsic defects of ZnO (0001) surface. (a) Gap states orbital mapping sideview of $V_O^0$ of ZnO(0001) with inset top view (spin-down=blue; spin-up=green). Gap states orbital mapping top-view of (b)$V_{Zn}^0$ (c)$A_{Zn}^0$ and (d) $A_O^0$ and (e) oxygen extrusion. (f) TDOS of the intrinsic defects ($V_O^0$, $V_{Zn}^0$, $A_{Zn}^0$, $A_O^0$). Summary of the native point defects in ZnO(0001) formation energies with comparison under both (g) O-poor and (h) rich chemical potential limits.

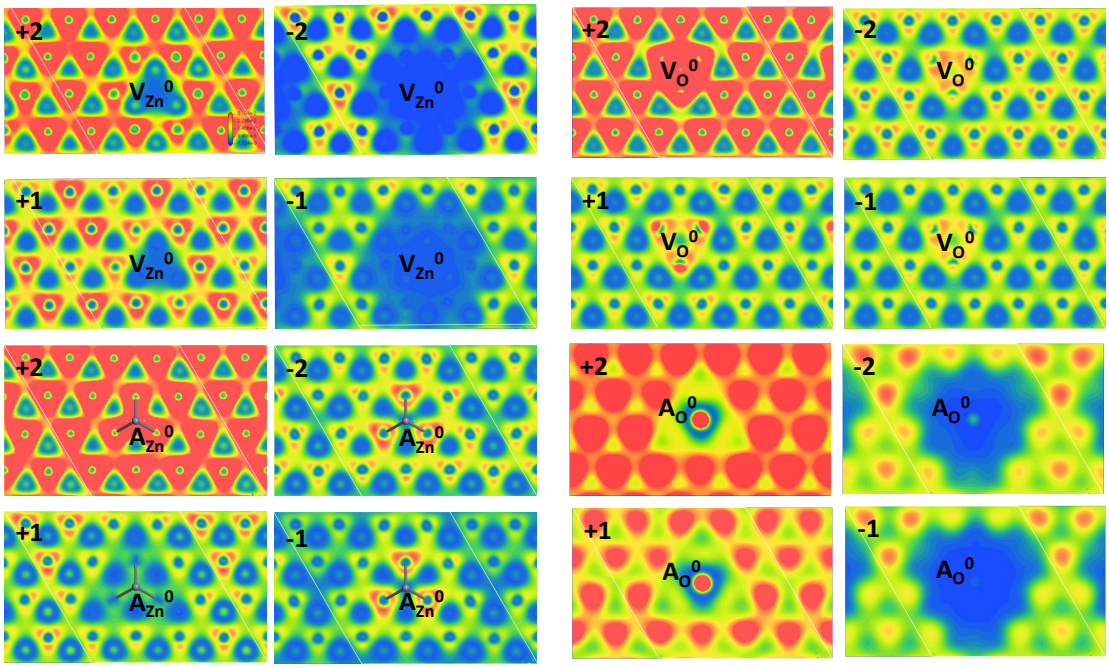


**Figure 7.** Theoretical simulation of the STM image of intrinsic defects under $V_{bias}$= +2.0, -2.0, +1.0, -1.0 eV, respectively.

**References:**


[1] Z. L. Wang; J. Song, *Science* **2006,** *312* (5771), 242-6.
[2] F.-R. Fan; Z.-Q. Tian; Z. Lin Wang, *Nano Energy* **2012,** *1* (2), 328-334.
[3] Y. Yang; W. Guo; K. C. Pradel; G. Zhu; Y. Zhou; Y. Zhang; Y. Hu; L. Lin; Z. L. Wang, *Nano Lett* **2012,** *12* (6), 2833-8.
[4] Y. Zhang; Y. Yang; Z. L. Wang, *Energy & Environmental Science* **2012,** *5* (5), 6850.
[5] X. Xue; W. Zang; P. Deng; Q. Wang; L. Xing; Y. Zhang; Z. L. Wang, *Nano Energy* **2015,** *13*, 414-422.
[6] G. Hu; Y. Zhang; L. Li; Z. L. Wang, *ACS Nano* **2018,** *12* (1), 779-785.
[7] S. Qiao; J. Liu; G. Fu; K. Ren; Z. Li; S. Wang; C. Pan, *Nano Energy* **2018,** *49*, 508-514.
[8] F. R. Fan; W. Tang; Z. L. Wang, *Adv Mater* **2016,** *28* (22), 4283-305.
[9] C. Wu; A. C. Wang; W. Ding; H. Guo; Z. L. Wang, *Advanced Energy Materials* **2019,** *9* (1), 1802906.
[10] X. Liang; T. Jiang; G. Liu; T. Xiao; L. Xu; W. Li; F. Xi; C. Zhang; Z. L. Wang, *Adv Funct Mater* **2019**, 1807241.
[11] F. Yi; L. Lin; S. Niu; P. K. Yang; Z. Wang; J. Chen; Y. Zhou; Y. Zi; J. Wang; Q. Liao; Y. Zhang; Z. L. Wang, *Adv Funct Mater* **2015,** *25* (24), 3688-3696.
[12] L. Lin; Q. S. Jing; Y. Zhang; Y. F. Hu; S. H. Wang; Y. Bando; R. P. S. Han; Z. L. Wang, *Energy & Environmental Science* **2013,** *6* (4), 1164-1169.
[13] C. Xu; B. Zhang; A. C. Wang; H. Zou; G. Liu; W. Ding; C. Wu; M. Ma; P. Feng; Z. Lin; Z. L. Wang, *ACS Nano* **2019**.
[14] C. Xu; Y. Zi; A. C. Wang; H. Zou; Y. Dai; X. He; P. Wang; Y.-C. Wang; P. Feng; D. Li; Z. L. Wang, *Adv Mater* **2018,** *30* (15), 1706790.
[15] C. Xu; A. C. Wang; H. Zou; B. Zhang; C. Zhang; Y. Zi; L. Pan; P. Wang; P. Feng; Z. Lin; Z. L. Wang, *Adv Mater* **2018,** *30* (38), e1803968.
[16] Q. Zhang; C. S. Dandeneau; X. Zhou; G. Cao, *Adv Mater* **2009,** *21* (41), 4087-4108.
[17] W. Wu; X. Wen; Z. L. Wang, *Science* **2013,** *340* (6135), 952-7.
[18] L. E. Greene; M. Law; J. Goldberger; F. Kim; J. C. Johnson; Y. Zhang; R. J. Saykally; P. Yang, *Angew Chem Int Ed Engl* **2003,** *42* (26), 3031-4.
[19] C. Soci; A. Zhang; B. Xiang; S. A. Dayeh; D. P. Aplin; J. Park; X. Y. Bao; Y. H. Lo; D. Wang, *Nano Lett* **2007,** *7* (4), 1003-9.
[20] L. Vayssieres, *Adv Mater* **2003,** *15* (5), 464-466.
[21] X. Y. Kong, *Science* **2004,** *303* (5662), 1348-1351.
[22] Z. W. Pan; Z. R. Dai; Z. L. Wang, *Science* **2001,** *291* (5510), 1947-9.
[23] X. Y. Kong; Z. L. Wang, *Nano Lett* **2003,** *3* (12), 1625-1631.
[24] X. Han; X. Zhou; Y. Jiang; Z. Xie, *J Mater Chem* **2012,** *22* (21), 10924.
[25] Y. Peng; M. Que; H. E. Lee; R. Bao; X. Wang; J. Lu; Z. Yuan; X. Li; J. Tao; J. Sun; J. Zhai; K. J. Lee; C. Pan, *Nano Energy* **2019,** *58*, 633-640.
[26] J. Lu; C. Xu; F. Li; Z. Yang; Y. Peng; X. Li; M. Que; C. Pan; Z. L. Wang, *ACS Nano* **2018**.
[27] M. Lazzeri; S. Piscanec; F. Mauri; A. C. Ferrari; J. Robertson, *Phys Rev Lett* **2005,** *95* (23), 236802.
[28] T. C. Damen; S. P. S. Porto; B. Tell, *Physical Review* **1966,** *142* (2), 570-574.
[29] C. T. White; T. N. Todorov, *Nature* **1998,** *393* (6682), 240-242.
[30] X. Wan; S. Y. Savrasov, *Nat Commun* **2014,** *5*, 4144.
[31] J. D. Budai; J. Hong; M. E. Manley; E. D. Specht; C. W. Li; J. Z. Tischler; D. L. Abernathy; A. H. Said; B. M. Leu; L. A. Boatner; R. J. McQueeney; O. Delaire, *Nature*

**2014,** *515* (7528), 535-9.
[32] X. Chen; X. Lu; S. Dubey; Q. Yao; S. Liu; X. Wang; Q. Xiong; L. Zhang; A. Srivastava, *Nature Physics* **2018**.
[33] J. Zhang; D. Li; R. Chen; Q. Xiong, *Nature* **2013,** *493* (7433), 504-8.
[34] R. P. Wang; G. Xu; P. Jin, *Physical Review B* **2004,** *69* (11).
[35] Y. J. Xing; Z. H. Xi; Z. Q. Xue; X. D. Zhang; J. H. Song; R. M. Wang; J. Xu; Y. Song; S. L. Zhang; D. P. Yu, *Appl Phys Lett* **2003,** *83* (9), 1689-1691.
[36] C. X. Xu; G. P. Zhu; X. Li; Y. Yang; S. T. Tan; X. W. Sun; C. Lincoln; T. A. Smith, *J Appl Phys* **2008,** *103* (9), 094303.
[37] F. Friedrich; N. H. Nickel, *Appl Phys Lett* **2007,** *91* (11), 111903.
[38] J. Jiang; R. Saito; A. Grüneis; G. Dresselhaus; M. S. Dresselhaus, *Chem Phys Lett* **2004,** *392* (4-6), 383-389.
[39] V. Perebeinos; J. Tersoff; P. Avouris, *Phys Rev Lett* **2005,** *94* (8), 086802.
[40] S. Piscanec; M. Lazzeri; F. Mauri; A. C. Ferrari; J. Robertson, *Phys Rev Lett* **2004,** *93* (18), 185503.
[41] B. Miller; J. Lindlau; M. Bommert; A. Neumann; H. Yamaguchi; A. Holleitner; A. Hogele; U. Wurstbauer, *Nat Commun* **2019,** *10* (1), 807.
[42] X. Wang; H. Zhang; R. Yu; L. Dong; D. Peng; A. Zhang; Y. Zhang; H. Liu; C. Pan; Z. L. Wang, *Adv Mater* **2015,** *27* (14), 2324-31.
[43] W. Wu; L. Wang; Y. Li; F. Zhang; L. Lin; S. Niu; D. Chenet; X. Zhang; Y. Hao; T. F. Heinz; J. Hone; Z. L. Wang, *Nature* **2014,** *514* (7523), 470-4.
[44] W. Wu; Z. L. Wang, *Nature Reviews Materials* **2016,** *1* (7).
[45] X. Cao; M. Zhang; J. Huang; T. Jiang; J. Zou; N. Wang; Z. L. Wang, *Adv Mater* **2018,** *30* (6).
[46] C. Xu; A. C. Wang; H. Zou; B. Zhang; C. Zhang; Y. Zi; L. Pan; P. Wang; P. Feng; Z. Lin; Z. L. Wang, *Adv Mater* **2018**, e1803968.
[47] Z. L. Wang; G. Zhu; Y. Yang; S. Wang; C. Pan, *Mater Today* **2012,** *15* (12), 532-543.
[48] H. Xu; L. Dong; X. Q. Shi; M. A. Van Hove; W. K. Ho; N. Lin; H. S. Wu; S. Y. Tong, *Phys. Rev. B* **2014,** *89* (23), 235403.